



## Wide-field time-of-flight measurements of highly scattering media

ANDRÉ STEFANOV,<sup>1,\*</sup> PASCAL TIJKORTE,<sup>1</sup> GIJS HANNINK,<sup>1,2</sup> LYNN ROTH,<sup>1</sup> AND MARTIN FRENZ<sup>1</sup>

<sup>1</sup>Institute of Applied Physics, University of Bern, 3012 Bern, Switzerland

<sup>2</sup>University of Twente, The Netherlands

\*andrei.stefanov@unibe.ch

Received 23 June 2023; revised 11 September 2023; accepted 7 October 2023; posted 30 October 2023; published 6 December 2023

We present a setup that makes use of a time-resolved single-photon camera to determine the scattering parameters of media. The measurement is realized in a non-contact way, both for the illumination laser and the detection. By fitting the time-of-flight acquired distributions at different spatial positions with the diffusion equation, we retrieve the reduced scattering coefficients of a highly diffusive isotropic reference media for wavelengths in the range from 540 to 840 nm. © 2023 Optica Publishing Group

<https://doi.org/10.1364/OL.498659>

**Introduction.** Light diffusion in strongly scattering media hampers the implementation of classical imaging methods. In the optical domain, clouds impair remote sensing, or the high scattering properties of biological tissues prevent direct imaging of the internal structures of biological samples. Methods have been devised to partially overcome those limitations. For instance, imaging through scattered media has been demonstrated by selecting non-scattered photons [1,2] or by shaping the spatial structure of the illumination beams [3,4]. On the other side, diffused light carries information about the microscopic properties of the scattering media, as the density of the scatterers, their sizes, shapes, and spatial distribution. Various techniques have been implemented depending on the observed light's degrees of freedom. For instance, dynamic light scattering and associated methods rely on the observation of spatial speckles [5], and polarimetric studies provide information on the symmetry of the scatterers [6]. Among the relevant properties of light, the time of flight of short optical pulses is strongly affected by scattering in highly diffusive media. Measuring such time of flight is fundamental for implementing various time-domain (TD) techniques [7], such as TD-near-infrared spectroscopy or TD diffuse optical tomography [8]. The relevant time information in a typical laboratory scale setup is of the order of tens to hundreds of picoseconds. This is why light detectors have to show sub-nanosecond time detection capabilities. Usually, this is achieved by time-correlated single-photon counting (TCSPC) with single-pixel photodetectors, such as avalanche photodiodes (APD) or photomultipliers. In that case, any spatial dependency is obtained by scanning. Arrays of single-photon avalanche detectors (SPAD) or more generally single-photon cameras with high temporal resolution can simultaneously measure both the position and the time of arrival for each detected photon. This

has been demonstrated for diffuse optical tomography [9], 3D imaging, and fluorescent lifetime imaging microscopy (FLIM) [10]. Recently, single-photon cameras allowed for non-scanning wide-field measurements, for instance with intensified CCD [11,12] or SPAD arrays [13].

Here we present the application of a time-resolved single-photon wide-field detection to estimate the scattering properties of the scattering medium in a backscattering configuration. The measurement is realized in a non-contact way, both for the illumination laser and for the detection, at a working distance of 60 mm. This renders the system suitable for a large range of applications, particularly for potential clinical applications. The capability of the system is validated by measuring the scattering by spherical-symmetric scatterers. The spatiotemporal dependency of the scattered photons is consistent with the analytical solution from the diffusion equation approximation, within its domain of validity.

**Experimental setup.** The experimental setup is shown in Fig. 1. The light from a wavelength-tunable picosecond laser (Solea Series by PicoQuant) is delivered through an optical fiber to the measurement system. The output of the fiber is collimated using a laser collimator (LC), and after being attenuated by neutral density (ND) filters, it illuminates a 50/50 beam splitter; 50% of the beam is reflected toward lens 4 (L4), and 50% of the light is absorbed by a black surface. L4 focuses the collimated laser beam onto the sample. The illumination beam is slightly tilted, so the specular reflection at the sample's surface can be imaged outside of the camera's field of view. The laser light diffuses in the sample and is backscattered toward L4. Thereafter, L3 and L2 create an intermediate imaging plane where a mask is mounted. The mask blocks the diffuse reflection at the illumination point. Subsequently, an iris can be placed in front of L2 to control the image intensity. Finally, L1 focuses the light on the time-resolved single-photon camera [LINCam from PHOTONSCORE GmbH (14)]. The camera's sensor has a size of 25 × 25 mm with an effective resolution of 4096 × 4096 pixels. All lenses in the setup have a focal distance of 60 mm, meaning a one-to-one imaging of the sample on the camera.

An external pulse/delay generator triggers both the laser and the camera. The repetition rate is set to 3 MHz and the illumination intensity is set by selecting ND filters and the iris aperture such that the camera is not saturated, i.e., by keeping the camera's detection count rate below 300 KHz.

The scattering media consists in dilutions of polystyrene spheres of 320 nm diameter (Magsphere Inc.) in pure water. The experiment was performed with dilutions ranging from 0.24% to 1.6% volume fraction.

The system records the spatial position and temporal bins of every detected photon. The temporal window is set to 12.5 ns with 4096 time-bins of 2.91 ps each. The system's overall jitter, or its instantaneous response function (IRF), is shown in Fig. 2 (red curve) and is estimated by illuminating a black absorbing paper. The directly reflected signal is fitted by an exponentially modified Gaussian function  $A \times \frac{1}{2} \exp\left(\frac{1}{2}(2\mu + \lambda\omega^2 - 2t)\right) \text{erfc}\left(\frac{\mu + \lambda\omega^2 - t}{\sqrt{2}\omega}\right) + B$  (see Fig. S1 of [Supplement 1](#)). The corresponding FWHM is 166 ps, essentially due to the laser pulse width of about 120 ps and the temporal response of the camera of 50 ps.

We build the spatiotemporal histogram proportional to the backscattered intensity  $h(x, y, t) = \eta R(x, y, t)$  from all the time-tagged single-photon detections. The  $4096 \times 4096$  pixels are binned to  $256 \times 256$ , and the 4096 time-bins to 2048. As the samples are isotropic in this study, the only relevant spatial dependency is the distance between the illumination position and the output point of the backscattered light. By averaging  $h(x, y, t)$  over rings of width  $dr = 0.2$  mm and with radii ranging from 1 to 6.5 mm, we obtain the radial and temporal distribution

$$h(r, t) = \frac{1}{2\pi r dr} \int_{r-dr/2}^{r+dr/2} dr' r' \int_0^{2\pi} d\theta h(r' \sin \theta, r' \cos \theta, t). \quad (1)$$

The experimentally measured distribution is further compared with the expected backscattered light as computed from the diffusion equation in a medium with refractive index  $n$  and a

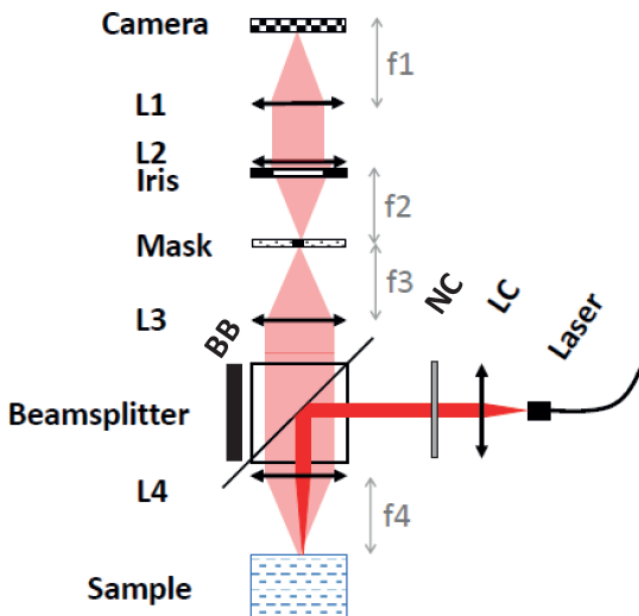


**Fig. 1.** Schematic of the experimental setup. A pulsed laser is focused on the sample surface by lenses LC and L4 and attenuated by neutral density filters (NC). The backscattered signal is imaged onto a single-photon camera by lenses L1, L2, L3, and L4, with an intermediate image plane where a blocking mask is placed. The light at the unused beam splitter's port is blocked by a beam blocker (BB).

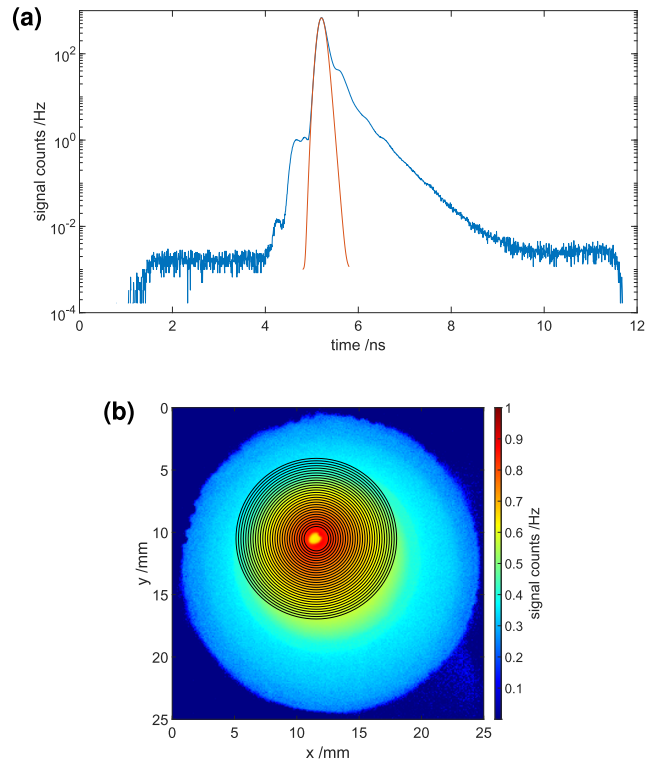


**Fig. 2.** Values of the spatiotemporal histogram integrated over space (a) and over time (b). The red curve in (a) is the estimated IRF of the system. The black circles in (b) show the selected radii and are centered on the illumination position.

reduced scattering coefficient  $\mu'_s$  [7]

$$R(r, t) = \frac{1}{16(\pi Dv)^{3/2} t^{5/2}} \exp(-\mu_a v t) \times \\ (z_0 \exp(-(r^2 + z_0^2)/(4Dvt)) \\ + (z_0 + 2z_b) \exp(-(r^2 + (z_0 + 2z_b)^2)/(4Dvt))), \quad (2)$$

with the diffusion coefficient  $D = 1/3(\mu'_s + \mu_a)$ ,  $v$  is the speed of light in the medium,  $z_0 = 1/\mu'_s$ , and  $z_b = 2D(1+f)/(1-f)$  with  $f$  the internal diffusive reflectivity estimated by the Fresnel reflection coefficient. We compute the reduced scattering coefficient from Mie theory from the scatterers parameters, refractive indices, size, and concentration, and assuming the absorption coefficient of water for all polystyrene samples [ $\mu_a = 0.0003 \text{ mm}^{-1}$  at 633 nm [\(15\)](#)].  $R(r, t)$  computed with those scattering and absorption coefficients is then convoluted with the measured IRF  $R_c(r, t) = \int dt R(r, t) \text{IRF}(t)$ .

Figure 2 illustrates an acquired histogram for a sample with a volume fraction of 0.24% of scatterers, measured at 633 nm illumination. Figure 2(a) shows the integration of the histogram over all spatial pixels  $h_t(t) = \int h(x, y, t) dx dy$ , together with the estimated IRF. On Fig. 2(b) the spatial distribution, integrated over all times, is shown with the radii set for further processing. The radial dependency of  $h(r, t)$  is strongly affected by the vignetting of the optical system, as seen in Fig. 2(a). This is why we use only the change of the temporal dependency at different radii to extract information about the scattering media. Therefore, for all measurements, we normalize  $h(r, t)$  to its maximum for each  $r$ ,  $\tilde{h}(r, t) = h(r, t)/\max_t h(r, t)$ . We apply the same normalization to the theoretical values  $R_c(r, t)$ .

**Results.** The experimentally determined values of  $\tilde{h}(r, t)$  at 633 nm are shown in Fig. 3, left column. The right column shows for comparison the normalized calculated backscattered light  $\tilde{R}_c(r, t)$ . We observe a good match between the observed and expected reflectivities. It has to be noted that for higher values of  $r$  and denser media, the signal becomes smaller, and thus the SNR decreases. In addition, some unwanted reflections of the illuminating beam in the optical system can lead to signals overlapping with the backscattered signal at spurious times and positions. As a further validation method, we performed a measurement with a standard TCSPC system. The results are in good agreement (see Figs. S2 and S3 in Supplement 1).

In the perspective of applying the measurement method to infer the scattering properties of the media, fitting the whole surface  $\tilde{h}(r, t)$  would not be robust enough because the width of the computed  $\tilde{h}(r, t)$  curve strongly depends on the IRF used for the convolution. However, the function  $t_{max}(r)$  is a suitable quantity to extract the reduced scattering coefficient from the data [16], where  $t_{max}(r)$  is the mode (the time corresponding to the maximum) of the temporal distribution for a fixed radius  $r$ . The scattering coefficient  $\mu'_s$  is obtained by fitting the function  $t_{max}(r)$  estimated from the data with the theoretical function  $R_c(r, t)$ , while the value of the absorption coefficient is assumed. The results of the fitting for the data of Fig. 3 are shown in Fig. 4. The error bars indicate the 95% confidence interval of the fitted values. The dashed line shows the expected scattering coefficients from Mie theory, while the shaded area shows the range of scattering coefficients assuming a  $\pm 5\%$  uncertainty in the scatterers' size. In the regime of low absorption, as here, uncertainty on the assumed absorption coefficient has little influence on the retrieved reduced scattering coefficient (see Fig. S4 of Supplement 1). Alternatively, we can fix the concentration of scatterers and scan over the illumination wavelength as shown on Fig. 5. While the overall dependency is clearly as expected, there seems to be a systematic shift that could be due to a systematic error in the estimation of the IRF. The effects of unwanted reflections are more relevant for longer wavelengths, for which they are more intense in relation to the backscattered signal.

**Conclusion.** The ability to spatially resolve backscattered photons' time of flight allows to retrieve the reduced scattering coefficient of highly diffusive media in a non-contact way without scanning stage. The results and retrieved scattering coefficients are compatible with the expected values in the diffusive regime. But it must be noted that the diffusion equation may not provide an accurate approximation for the low-concentration samples, in particular at close distance to the illumination. The non-contact geometry for illumination and detection makes the system well suited for a wide range of future applications. However, compared to contact fiber-based methods, it introduces additional sources of error in the measurements. In particular, multiple reflections of the illumination beam in the beam splitter and other optical surfaces are superimposed with the backscattered signal. Those reflections distort the measured function  $h(x, y, t)$ , leading to errors in the fitted scattering coefficients. Those effects will be reduced by optimizing the optical design. The ultimate sensitivity of the methods is given by the saturation rate of the detector, as in conventional TCSPC methods. Here parallelized sensors with higher saturation rates, such as SPAD arrays, could provide very high count rates.

While the method was demonstrated with isotropic media, spatial anisotropy in the scattering will produce a noncircular

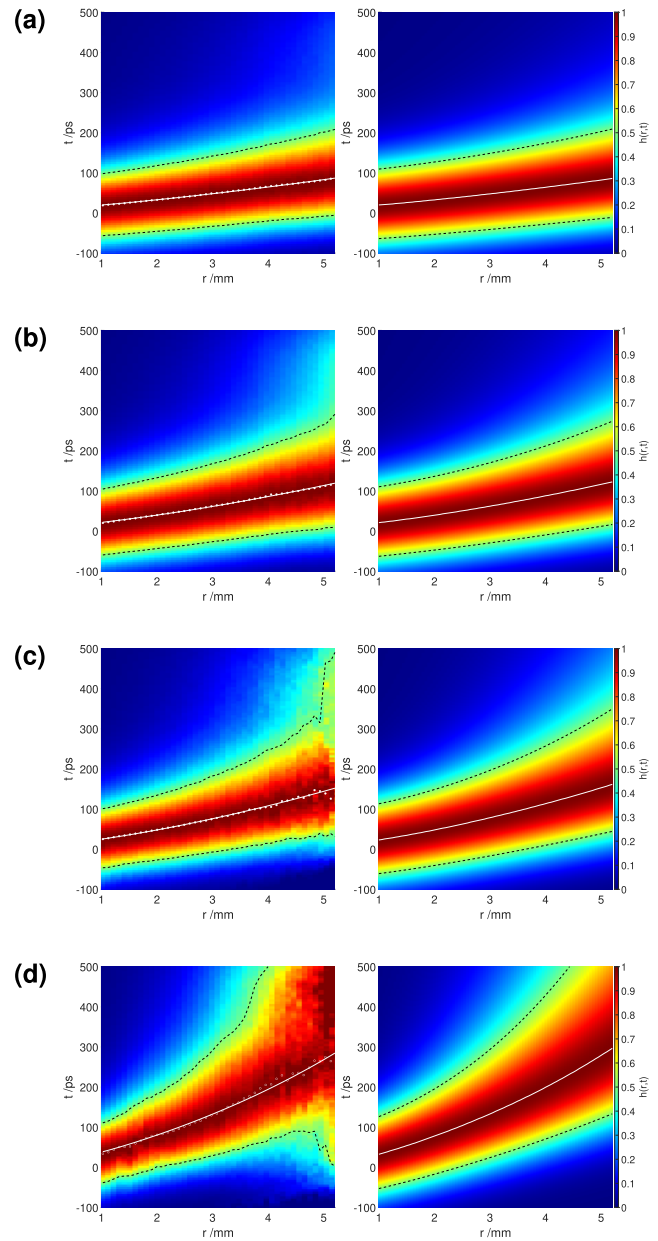


**Fig. 3.** Measured (left) and calculated (right) values for the back-scattered intensities  $\tilde{h}(r, t)$  as a function of the distance to the illumination point and of time, for various concentrations of the scatterers, expressed in volume fraction: (a) 0.24%, (b) 0.45%, (c) 0.69%, and (d) 1.59%. On the measured data, the white dots indicate the most probable value of the temporal distribution measured at each radius, and the continuous white line shows a fit of those positions, while the dash lines indicate the FWHM value at each radius. The same quantities are also shown for the calculated values.

backscattering pattern. As a consequence, the angular dependency of the backscattered intensity can be directly observed, which will give direct insights into the microscopic structure of the scatterers [17–20].

The demonstration of the presented setup opens the way for the direct investigation of the spatiotemporal properties of the backscattered light in non-isotropic scattering media, in particular for the identification of the microscopic structures of biological tissues.

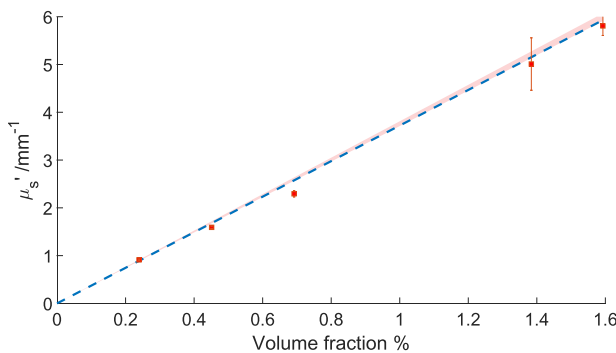


**Fig. 4.** Determined (red dots) and expected values (dashed blue line) of the reduced scattering coefficient  $\mu'_s$  as a function of the volume fraction of the scatterers at 630 nm. The shaded area indicates the range of values assuming a  $\pm 5\%$  variation of the scatters size.

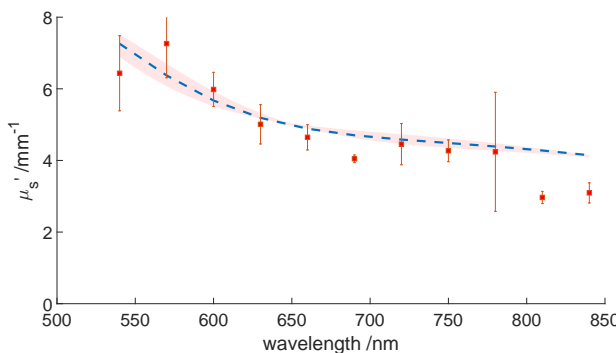


**Fig. 5.** Determined (red dots) and expected values (dashed blue line) of the reduced scattering coefficient  $\mu'_s$  as a function of the wavelength, at a volume fraction of 1.38%. The shaded area indicates the range of values assuming a  $\pm 5\%$  variation of the size of the scatters.

**Funding.** Schweizerischer Nationalfonds zur Förderung der Wissenschaftlichen Forschung (200021\_212872).

**Acknowledgment.** This work is supported by the Swiss National Science Foundation (Grant No. 200021\_212872).

**Disclosures.** The authors declare no conflicts of interest.

**Data availability.** The data that support the findings of this study are available from the corresponding author upon reasonable request.

**Supplemental document.** See [Supplement 1](#) for supporting content.

## REFERENCES

- V. Gopal, S. Mujumdar, H. Ramachandran, and A. K. Sood, *Opt. Commun.* **170**, 331 (1999).
- S. Farsiu, J. Christofferson, B. Eriksson, P. Milanfar, B. Friedlander, A. Shakouri, and R. Nowak, *Appl. Opt.* **46**, 5805 (2007).
- S. Rotter and S. Gigan, *Rev. Mod. Phys.* **89**, 015005 (2017).
- Y. Seokchan, K. Moonseok, J. Mooseok, C. Youngwoon, C. Wonjun, K. Sungsam, and C. Wonshik, *Nat. Rev. Phys.* **2**, 141 (2020).
- P. Zakharov and F. Scheffold, in *Light Scattering Reviews* **4**, A. A. Kokhanovsky, ed. (Springer, 2009), p. 433.
- A. Jain, L. Ulrich, M. Jaeger, P. Schucht, M. Frenz, and H. G. Akarcay, *Biomed. Opt. Express* **12**, 4452 (2021).
- Y. Yamada, H. Suzuki, and Y. Yamashita, *Appl. Sci.* **9**, 1127 (2019).
- Y. Hoshi and Y. Yamada, *J. Biomed. Opt.* **21**, 091312 (2016).
- A. Lyons, F. Tonolini, A. Boccolini, A. Repetti, R. Henderson, Y. Wiaux, and D. Faccio, *Nat. Photonics* **13**, 575 (2019).
- Y. Prokazov, E. Turbin, A. Weber, R. Hartig, and W. Zuschratter, *J. Instrum.* **9**, C12015 (2014).
- Q. Zhao, L. Spinelli, A. Bassi, G. Valentini, D. Contini, A. Torricelli, R. Cubeddu, G. Zaccanti, F. Martelli, and A. Pifferi, *Biomed. Opt. Express* **2**, 705 (2011).
- P. Sawosz, M. Kaprzak, W. Weigl, A. Borowska-Solonyko, P. Krajewski, N. Zolek, B. Ciszek, R. Maniewski, and A. Liebert, *Phys. Med. Biol.* **57**, 7973 (2012).
- J. Jiang, A. D. Costanzo Mata, S. Lindner, E. Charbon, M. Wolf, and A. Kalyanov, *Biomed. Opt. Express* **11**, 5470 (2020).
- Y. Prokazov, E. Turbin, M. Vitali, A. Herzog, B. Michaelis, W. Zuschratter, and K. Kemnitz, *Nucl. Instrum. Methods Phys. Res., Sect. A* **604**, 221 (2009).
- R. M. Pope and E. S. Fry, *Appl. Opt.* **36**, 8710 (1997).
- M. S. Patterson, B. Chance, and B. C. Wilson, *Appl. Opt.* **28**, 2331 (1989).
- J. Heino, S. Arridge, J. Sikora, and E. Somersalo, *Phys. Rev. E* **68**, 031908 (2003).
- A. Kienle, F. K. Forster, and R. Hibst, *Opt. Lett.* **29**, 2617 (2004).
- A. Kienle, *Phys. Rev. Lett.* **98**, 218104 (2007).
- M. Menzel, M. Axer, H. De Raedt, I. Costantini, L. Silvestri, F. S. Pavone, K. Amunts, and K. Michielsen, *Phys. Rev. X* **10**, 021002 (2020).